LETTER

doi:10.1038/nature16455

Partially oxidized atomic cobalt layers for carbon dioxide electroreduction to liquid fuel

Shan Gao[1], Yue Lin[1], Xingchen Jiao[1], Yongfu Sun[1,2], Qiquan Luo[1], Wenhua Zhang[1], Dianqi Li[1], Jinlong Yang[1] & Yi Xie[1,2]

Electroreduction of CO_2 into useful fuels, especially if driven by renewable energy, represents a potentially 'clean' strategy for replacing fossil feedstocks and dealing with increasing CO_2 emissions and their adverse effects on climate[1–4]. The critical bottleneck lies in activating CO_2 into the $CO_2^{\bullet-}$ radical anion or other intermediates that can be converted further, as the activation usually requires impractically high overpotentials. Recently, electrocatalysts based on oxide-derived metal nanostructures have been shown[5–8] to enable CO_2 reduction at low overpotentials. However, it remains unclear how the electrocatalytic activity of these metals is influenced by their native oxides, mainly because microstructural features such as interfaces and defects[9] influence CO_2 reduction activity yet are difficult to control. To evaluate the role of the two different catalytic sites, here we fabricate two kinds of four-atom-thick layers: pure cobalt metal, and co-existing domains of cobalt metal and cobalt oxide. Cobalt mainly produces formate ($HCOO^-$) during CO_2 electroreduction; we find that surface cobalt atoms of the atomically thin layers have higher intrinsic activity and selectivity towards formate production, at lower overpotentials, than do surface cobalt atoms on bulk samples. Partial oxidation of the atomic layers further increases their intrinsic activity, allowing us to realize stable current densities of about 10 milliamperes per square centimetre over 40 hours, with approximately 90 per cent formate selectivity at an overpotential of only 0.24 volts, which outperforms previously reported metal or metal oxide electrodes evaluated under comparable conditions[1,2,6,7,10]. The correct morphology and oxidation state can thus transform a material from one considered nearly non-catalytic for the CO_2 electroreduction reaction into an active catalyst. These findings point to new opportunities for manipulating and improving the CO_2 electroreduction properties of metal systems, especially once the influence of both the atomic-scale structure and the presence of oxide are mechanistically better understood.

To explore the catalytic role of metal sites and metal oxide sites, we first construct a system containing a 4-atom-thick metal layer and then create the corresponding metal oxide on its surface. The atomic thickness of this model system ensures that most of the metal atoms are present as either surface atoms or surface ions[11,12], so we can explore how the presence of a surface oxide influences the catalytic activity of the corresponding metal. We focus on cobalt (Co) because metals with loosely bonded *d* electrons and the resulting high electrical conductivity are promising for CO_2 reduction[13], and because both Co and its oxide are widely used catalysts[14–16]. Importantly, the spontaneous oxidation of Co nanostructures in air is relatively slow[17], and the use of other gases makes it possible to manipulate and control the oxidation process[18]. However, strong in-plane bonds and the lack of an intrinsic driving force for two-dimensional anisotropic growth make the synthesis of Co atomic layers and the controlled conversion of such layers into partially oxidized atomic layers very challenging.

We produced freestanding 4-atom-thick Co sheets with and without surface Co oxide using a ligand-confined growth strategy, in which the use of dimethylformamide and *n*-butylamine proved crucial for reducing the metal ions and enforcing a sheet-like morphology, respectively (Extended Data Fig. 1). The starting reagent cobalt(III) acetylacetonate, $Co(acac)_3$, initially hydrolyses into $[Co(H_2O)_6]^{3+}$, on which *n*-butylamine is adsorbed to reduce surface energy and avoid aggregation (Fig. 1a and Extended Data Fig. 2a) until sheet-like products gradually appear during the subsequent condensation process (Extended Data Fig. 2b). Controlled fabrication of either partially oxidized or pure Co atomic layers is achieved by using dimethylformamide to gradually reduce the cobalt ions[19] (Fig. 1a), illustrated by the products obtained at 220 °C after reaction times of either 3 h or 48 h.

Transmission electron microscope (TEM) images of the product obtained after 3 h reveal a sheet-like morphology, while the powder X-ray diffraction (XRD) pattern can be readily indexed to hexagonal Co (Extended Data Fig. 3a, b). High-resolution TEM images demonstrate that the majority of these two-dimensional sheets correspond to the [001]-oriented hexagonal Co (Fig. 2a, b and Extended Data Fig. 3c), with average sheet thickness of 0.84 nm determined with atomic force microscopy (Fig. 1b, c), close to the 0.82-nm thickness of a 4-atom-thick Co slab along the [001] direction. Lateral high-angle annular dark-field scanning transmission electron microscopy (HAADF-STEM) imaging confirms the 4-atom layer thickness (Fig. 1d–g).

However, the high-resolution TEM images in Fig. 2a and c also reveal the presence of another distinct structural domain with an interplanar spacing of 0.205 nm and dihedral angle of 90°. This domain corresponds to the (400) plane of cubic Co_3O_4, which is embedded in the metallic Co lattice (see schemes in Fig. 2d and e; another high-resolution TEM image from a larger area of an individual sheet showing Co oxide embedded in Co metal is provided in Extended Data Fig. 3c). Elemental mapping (Fig. 2f–h) supports the conclusion that Co metal and Co oxide co-exist in this sample. This is also consistent with the observation of micro-Raman peaks at 482 cm^{-1}, 523 cm^{-1}, 621 cm^{-1} and 694 cm^{-1} (Fig. 2i), which correspond to a Co_3O_4 phase[20] and that disappear upon increasing the reaction time to 48 h. Taken together, these observations demonstrate that the 4-atom-thick Co sheets obtained after 3 h at 220 °C contain some Co oxide, whereas increasing the reaction time to 48h leads to the formation of pure Co 4-atom-thick layers.

To characterize the performance of the materials as CO_2 reduction electrocatalysts, they were loaded onto a glassy carbon electrode that served as the working electrode; linear sweep voltammetry was carried out using a CO_2-saturated 0.1 M Na_2SO_4 solution in a three-electrode set-up. Use of the partially oxidized Co 4-atom-thick layers generates a current density of 10.59 mA cm^{-2} at −0.85 V versus a saturated calomel electrode (SCE) (Fig. 3a), roughly 10, 40 and 260 times larger than the current densities obtained with the pure-Co 4-atom-thick layer (Extended Data Fig. 4), the partially oxidized bulk Co and bulk Co (Extended Data Fig. 5), respectively.

Quantification of the solution-phase products by ^1H nuclear magnetic resonance (NMR) shows that of the four samples, the partially

[1]Hefei National Laboratory for Physical Sciences at Microscale, Collaborative Innovation Center of Chemistry for Energy Materials, University of Science and Technology of China, Hefei, Anhui 230026, China. [2]Hefei Science Center of CAS, Hefei, Anhui 230061, China.

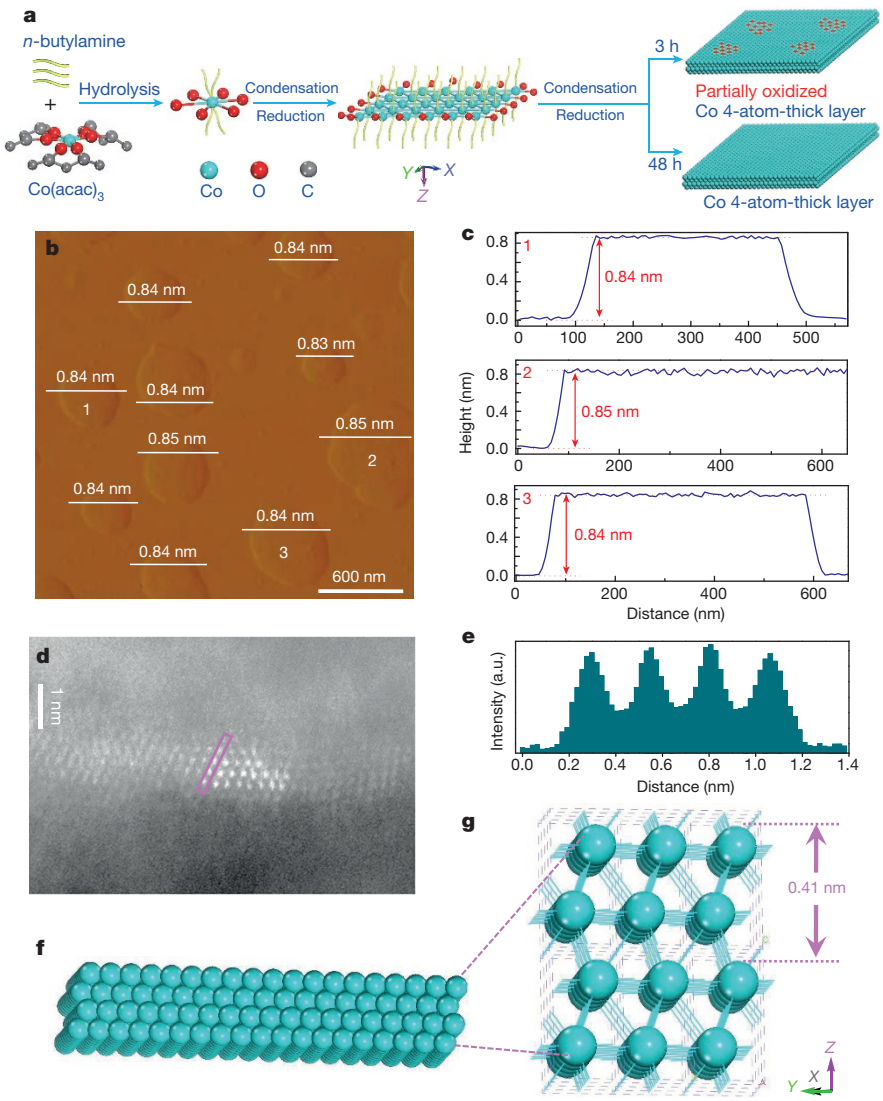

Figure 1 | Synthetic scheme and characterizations of Co 4-atom-thick layers with and without surface oxide. a, Schematic formation process of the partially oxidized and pure-Co 4-atomic-layer, respectively. **b**–**g**, Characterizations for the partially oxidized Co 4-atomic-layers: atomic force microscopy image (**b**) and the corresponding height profiles (**c**) (we note that the numbers from 1 to 3 in **c** correspond to the numbers from 1 to 3 in **b**), lateral HAADF-STEM image (**d**) and the corresponding intensity profile along the pink rectangle in **d**, directly showing the 4-atom thickness of the layer (**e**), and the corresponding crystal structures (**f**, **g**). a.u., arbitrary units.

oxidized Co 4-atom-thick layers attain the highest Faradaic efficiency for formate production of 90.1% at −0.85 V versus SCE (Fig. 3b and Extended Data Fig. 6a, b)[21]. H_2 evolution, quantified by gas chromatography, accounts for the remaining ~10% of the charges passed. The linear sweep voltammetry curves in N_2-saturated 0.1 M Na_2SO_4 solution indicate that the ultrathin structure and the presence of surface Co oxide also increase the H_2O reduction activity of the catalyst system (Fig. 3a). A $^{13}CO_2$ labelling experiment involving the same set-up and 8-h electrolysis yielded a product that generates an obvious ^{13}C NMR peak at 168.5 parts per million, attributed to $H^{13}COO^-$, and a ^1H NMR doublet, corresponding to the proton coupled to the ^{13}C of $H^{13}COO^-$ (Extended Data Fig. 6c, d)[22], confirming that formate is indeed derived from CO_2.

Taking the reduction potential of $E = -0.61$ V versus SCE for the $CO_2/HCOO^-$ couple in CO_2-saturated 0.1 M Na_2SO_4 solution[3], the potential of −0.85 V versus SCE used in our experiments corresponds to an overpotential of 0.24 V. To the best of our knowledge, achieving at such a low overpotential a current density as high as 10.59 mA cm^{-2} and 90.1% formate selectivity has not been possible with any of the previously reported metal or metal oxide electrodes evaluated under comparable conditions[1,2,6,7,10]. Intriguingly, when using the partially oxidized Co 4-atom-thick layers as the working electrode, CO_2 reduction initiated at −0.68 V versus SCE with a measured Faradaic efficiency for formate formation of 2.3% (Fig. 3a, b). This corresponds to an overpotential of only 0.07 V, comparable to that achieved with highly active Pd nanoparticles dispersed on a carbon support[21].

The remarkably enhanced activity of the ultrathin nanostructured catalysts is partly due to their increased electrochemical surface area (ECSA; see Methods for details) that provides a larger number of catalytically active sites. The fivefold ECSA increase from bulk Co to Co 4-atom-thick layers is an important contributor to the 26-fold increase in catalytic activity (Fig. 3a, c). Interestingly, the partially oxidized Co 4-atom-thick layers exhibited nearly the same ECSA as the Co 4-atom-thick layers, yet also a tenfold higher catalytic activity that must therefore be due to the presence of intrinsically more active sites associated with the Co oxide. This conclusion is supported by the relative performance of partially oxidized bulk Co and intact bulk Co (Fig. 3a, c), and by the finding that catalytic current densities gradually increase as the amount of Co oxide in the Co 4-atom-thick layers increases (Extended Data Fig. 7). During 40-h electrocatalysis tests, the partially oxidized Co 4-atom-thick layers show negligible decay in current density while maintaining a formate Faradaic efficiency of approximately 90% (Fig. 3d and Extended Data Fig. 6b). This suggests good stability, which is also confirmed by XRD, Raman and TEM characterization before and after use (Extended Data Fig. 8). Stability testing for Co 4-atom-thick layers and bulk Co also indicates that they do not undergo obvious oxidation or corrosion during long-term electrolysis (Extended Data Figs 9 and 10).

Volumetric CO_2 adsorption measurement, carried out to explore the reason for the enhanced electrocatalytic activity observed, reveals that the Co 4-atom-thick layer system absorbs more CO_2 than its bulk counterpart and that partial oxidation increases CO_2 adsorption capacity

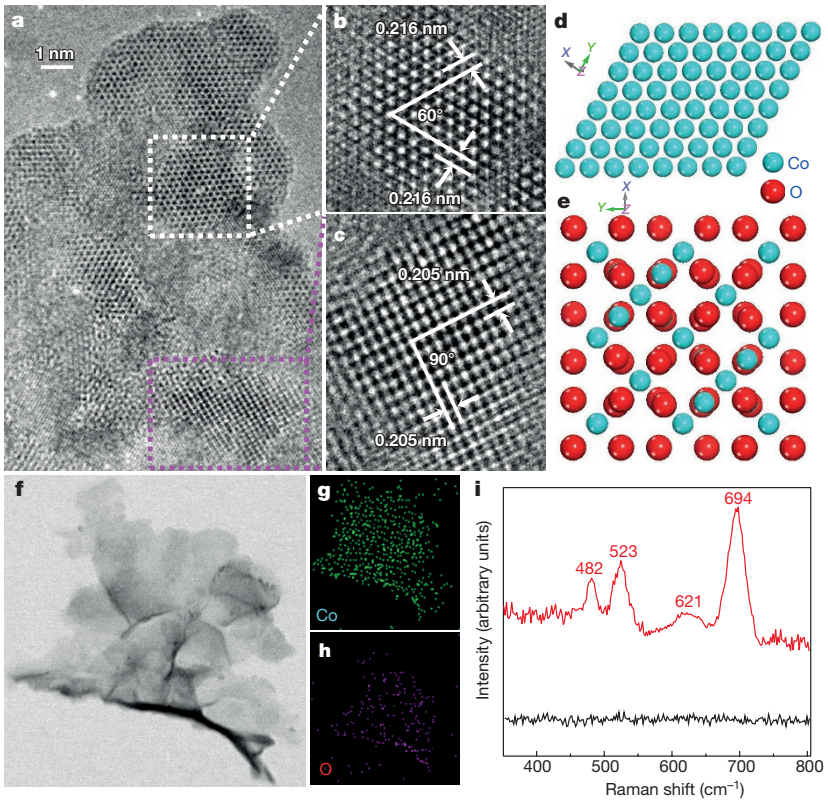

Figure 2 | Characterizations for the partially oxidized Co 4-atom-thick layers obtained at 220 °C for 3 h. **a**, High-resolution TEM image. **b**, **c**, Enlarged high-resolution TEM images. **d**, **e**, The related schematic atomic models, clearly showing distinct atomic configuration corresponding to hexagonal Co and cubic Co_3O_4. **f**–**h**, Elemental mapping. **i**, Micro-Raman spectra for the products obtained at 220 °C for 3 h (red line) and 48 h (black line).

further (Fig. 4a). This suggests that the change in oxidation state and increase in surface area synergistically favour CO_2 adsorption, the prerequisite first event before further reduction reactions can take place. It is commonly accepted that on metal electrodes[3,5–8,23,24], the adsorbed CO_2 is initially reduced to the $CO_2^{\bullet-}$ intermediate, which could then react further according to:

$$CO_2\,(g) + * \rightarrow CO_2* \quad (1)$$

$$CO_2* + e^- \rightarrow CO_2^{\bullet-}* \quad (2)$$

$$CO_2^{\bullet-}* + H^+ + e^- \rightarrow HCOO^-* \quad (3)$$

$$HCOO^-* \rightarrow HCOO^- + * \quad (4)$$

where the asterisk denotes a catalytically active site and e^- is an electron. ECSA-corrected Tafel slopes for formate production (see Methods for details) catalysed by the partially oxidized bulk Co and by bulk Co are both close to 118 mV per decade of current (Fig. 4b), indicative of the involvement of a rate-limiting $1e^-$ transfer from CO_2 to $CO_2^{\bullet-}$ (refs 5–8).

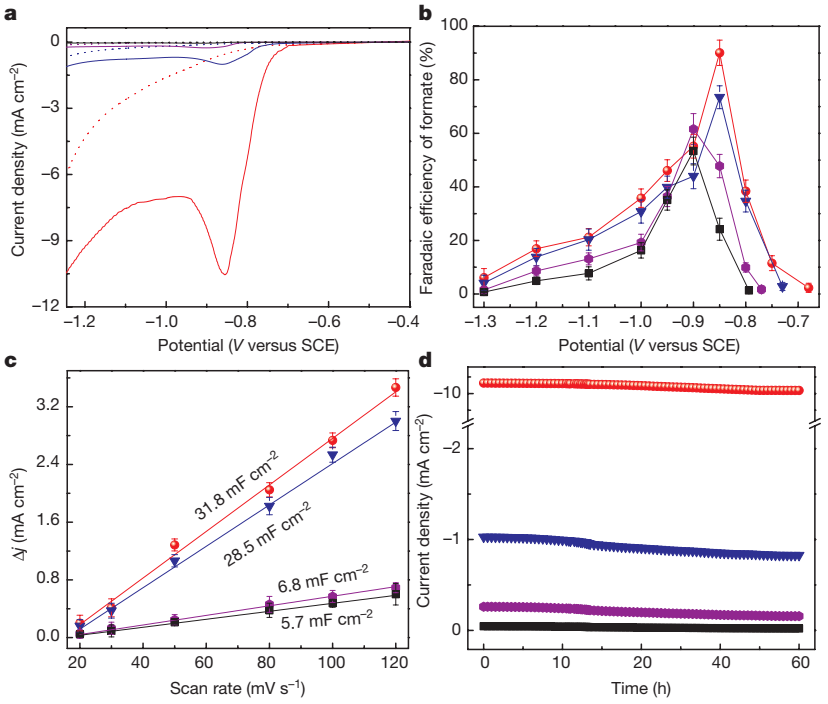

Figure 3 | Electroreduction of CO_2 to formate. Data are shown for partially oxidized Co 4-atom-thick layers (red), Co 4-atom-thick layers (blue), partially oxidized bulk Co (violet) and bulk Co (black). **a**, Linear sweep voltammetric curves in a CO_2-saturated (solid line) and N_2-saturated (dashed line) 0.1 M Na_2SO_4 aqueous solution. **b**, Faradaic efficiencies of formate at each given potential for 4 h. **c**, Charging current density differences Δj plotted against scan rates. **d**, Chrono-amperometry results at the corresponding potentials (in **b**) with the highest Faradaic efficiencies. The error bars in **b** and **c** represent the standard deviations of five independent measurements of the same sample.

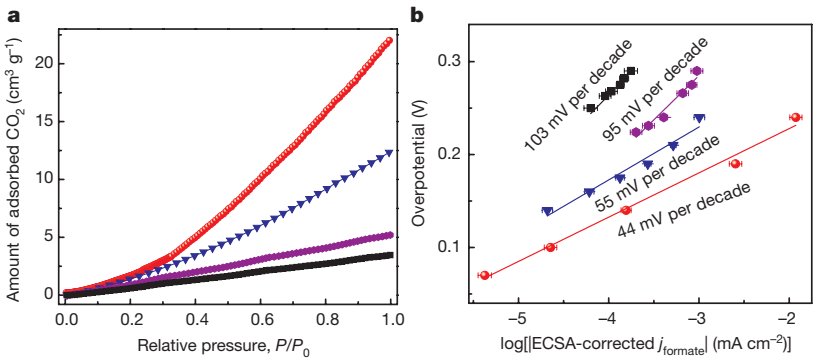

Figure 4 | Comparison of CO_2 adsorption amount and ECSA-corrected Tafel plots. Data are shown for the partially oxidized Co 4-atom-thick layers (red), Co 4-atom-thick layers (blue), partially oxidized bulk Co (violet) and bulk Co (black). **a**, CO_2 adsorption isotherms. **b**, ECSA-corrected Tafel plots for formate production. $j_{formate}$ is the partial current density of producing formate. The error bars in **b** represent the standard deviations of five independent measurements of the same sample.

In contrast, corresponding Tafel slopes of close to 59 mV per decade obtained with the partially oxidized Co 4-atomic-layers and Co 4-atomic-layers are compatible with a reduction mechanism encompassing a fast pre-equilibrium involving $1e^-$ transfer to form $CO_2^{\bullet-}$ and a subsequent slower chemical reaction as the rate-determining step[5–8]. If this is indeed the case, it appears that Co atoms confined in atomic layers are able to facilitate CO_2 activation by stabilizing the $CO_2^{\bullet-}$ intermediate more effectively than can be achieved by their bulk counterpart. We speculate that the further decrease in Tafel slope from 55 mV per decade to 44 mV per decade and the lowering of the onset potential from 0.73 V to 0.68 V upon partial oxidation of the Co 4-atom-thick layers (Figs 3b and 4b) might be due to Co oxide facilitating the rate-determining chemical reaction, probably the H^+ transfer step (equation (3)). We note, however, that the reaction mechanism remains uncertain and that further efforts are needed to gain in-depth understanding of the individual steps involved.

Our synthetic strategy has allowed us to produce a well controlled model system to explore the influence of both atomic-scale structure and the presence of an oxide on the activity of a metal catalyst. ECSA-corrected Tafel plots and Faradaic efficiencies clearly demonstrate that Co-based catalysts in the form of 4-atom-thick layers exhibit higher intrinsic activity and selectivity for formate production at lower overpotentials than the bulk material, and that partial oxidation improves the intrinsic activity of the system significantly further. Thus the appropriate morphology and oxidation state can transform a material considered nearly non-catalytic for CO_2 reduction into a very active and robust catalyst, calling for a re-thinking of accepted strategies for developing efficient CO_2 electroreduction catalysts.

Online Content Methods, along with any additional Extended Data display items and Source Data, are available in the online version of the paper; references unique to these sections appear only in the online paper.

Received 10 March; accepted 10 November 2015.

1. Zhang, S., Kang, P. & Meyer, T. J. Nanostructured tin catalysts for selective electrochemical reduction of carbon dioxide to formate. *J. Am. Chem. Soc.* **136,** 1734–1737 (2014).
2. Huang, X. F., Cao, T. C., Liu, M. C. & Zhao, G. H. Mg-doped $CuFeO_2$ photocathodes for photoelectrochemical reduction of carbon dioxide. *J. Phys. Chem. C* **117,** 26432–26440 (2013).
3. Rosen, B. A. *et al.* Ionic liquid-mediated selective conversion of CO_2 to CO at low overpotentials. *Science* **334,** 643–644 (2011).
4. Zhang, S. *et al.* Polyethylenimine-enhanced electrocatalytic reduction of CO_2 to formate at nitrogen-doped carbon nanomaterials. *J. Am. Chem. Soc.* **136,** 7845–7848 (2014).
5. Chen, Y. H., Li, C. W. & Kanan, M. W. Aqueous CO_2 reduction at very low overpotential on oxide-derived Au nanoparticles. *J. Am. Chem. Soc.* **134,** 19969–19972 (2012).
6. Li, C. W., Ciston, J. & Kanan, M. W. Electroreduction of carbon monoxide to liquid fuel on oxide-derived nanocrystalline copper. *Nature* **508,** 504–507 (2014).
7. Li, C. W. & Kanan, M. W. CO_2 reduction at low overpotential on Cu electrodes resulting from the reduction of thick Cu_2O films. *J. Am. Chem. Soc.* **134,** 7231–7234 (2012).
8. Chen, Y. H. & Kanan, M. W. Tin oxide dependence of the CO_2 reduction efficiency on tin electrodes and enhanced activity for tin/tin oxide thin-film catalysts. *J. Am. Chem. Soc.* **134,** 1986–1989 (2012).
9. Sun, Y. F., Gao, S., Lei, F. C., Xiao, C. & Xie, Y. Ultrathin two-dimensional inorganic materials: new opportunities for solid state nanochemistry. *Acc. Chem. Res.* **48,** 3–12 (2015).
10. Watkins, J. D. & Bocarsly, A. B. Direct reduction of carbon dioxide to formate in high-gas-capacity ionic liquids at post-transition-metal electrodes. *ChemSusChem* **7,** 284–290 (2014).
11. Sun, Y. F. *et al.* Pits confined in ultrathin cerium(IV) oxide for studying catalytic centers in carbon monoxide oxidation. *Nature Commun.* **4,** 2899 (2013).
12. Sun, Y. F. *et al.* Fabrication of flexible and freestanding zinc chalcogenide single layers. *Nature Commun.* **3,** 1057 (2012).
13. Asadi, M. *et al.* Robust carbon dioxide reduction on molybdenum disulphide edges. *Nature Commun.* **5,** 4470 (2014).
14. Xie, X. W., Li, Y., Liu, Z. Q., Haruta, M. & Shen, W. J. Low-temperature oxidation of CO catalysed by Co_3O_4 nanorods. *Nature* **458,** 746–749 (2009).
15. Roy, S. C., Varghese, O. K., Paulose, M. & Grimes, C. A. Toward solar fuels: photocatalytic conversion of carbon dioxide to hydrocarbons. *ACS Nano* **4,** 1259–1278 (2010).
16. Sun, Y. F. *et al.* Atomically-thin non-layered cobalt oxide porous sheets for highly efficient oxygen-evolving electrocatalysts. *Chem. Sci.* **5,** 3976–3982 (2014).
17. Salavati-Niasari, M., Fereshteh, Z. & Davar, F. Synthesis of cobalt nanoparticles from [bis(2-hydroxyacetophenato)cobalt(II)] by thermal decomposition. *Polyhedron* **28,** 1065–1068 (2009).
18. Rojas, T. C. *et al.* Preparation, characterization and thermal evolution of oxygen passivated nanocrystalline cobalt. *J. Mater. Chem.* **9,** 1011–1017 (1999).
19. Huang, X. Q. *et al.* Freestanding palladium nanosheets with plasmonic and catalytic properties. *Nature Nanotechnol.* **6,** 28–32 (2011).
20. Varghese, B. *et al.* Co_3O_4 nanostructures with different morphologies and their field-emission properties. *Adv. Funct. Mater.* **17,** 1932–1939 (2007).
21. Min, X. Q. & Kanan, M. W. Pd-catalyzed electrohydrogenation of carbon dioxide to formate: high mass activity at low overpotential and identification of the deactivation pathway. *J. Am. Chem. Soc.* **137,** 4701–4708 (2015).
22. Tamaki, Y., Morimoto, T., Koike, K. & Ishitani, O. Photocatalytic CO_2 reduction with high turnover frequency and selectivity of formic acid formation using Ru(II) multinuclear complexes. *Proc. Natl Acad. Sci. USA* **109,** 15673–15678 (2012).
23. Kumar, B. *et al.* Renewable and metal-free carbon nanofibre catalysts for carbon dioxide reduction. *Nature Commun.* **4,** 2819 (2013).
24. Gattrell, M., Gupta, N. & Co, A. A review of the aqueous electrochemical reduction of CO_2 to hydrocarbons at copper. *J. Electroanal. Chem.* **594,** 1–19 (2006).

Acknowledgements This work was financially supported by the National Basic Research Program of China (grant number 2015CB932302), the National Nature Science Foundation (grant numbers 21422107, 21331005, 91422303, 21201157 and 11321503), the Program for New Century Excellent Talents in University (grant number NCET-13-0546), the Youth Innovation Promotion Association of CAS (grant number CX2340000100), the Chinese Academy of Science (grant number XDB01020300), the Fundamental Research Funds for the Central Universities (grant number WK2340000063) and the Scientific Research Grant of the Hefei Science Center of CAS (grant numbers 2015HSC-UE006 and 2015HSC-UP015).

Author Contributions Y.X., Y.S. and S.G. conceived the idea and co-wrote the paper. Y.S., S.G., Y.L., X.J. and D.L. carried out the sample synthesis, characterization and CO_2 reduction measurement. Y.S., S.G., Q.L., W.Z. and J.Y. discussed the catalytic process. All the authors contributed to the overall scientific interpretation and edited the manuscript.

Author Information Reprints and permissions information is available at www.nature.com/reprints. The authors declare no competing financial interests. Readers are welcome to comment on the online version of the paper. Correspondence and requests for materials should be addressed to Y.X. (yxie@ustc.edu.cn) and Y.S. (yfsun@ustc.edu.cn).

METHODS

Synthesis of partially oxidized Co 4-atom-thick layers. In a typical procedure, 100 mg $Co(acac)_3$ was added into a solution of 20 ml dimethylformamide, 4 ml H_2O and 1 ml *n*-butylamine. After vigorous stirring for 15 min, the mixture was transferred into a 40-ml Teflon-lined autoclave (before this experiment, the autoclave was initially treated with 20 ml *n*-butylamine at 120 °C for 6 h, and then treated with 35 ml H_2O at 120 °C for 12 h), sealed and heated at 220 °C for 3 h. The system was allowed to cool down to room temperature naturally, and the final product was collected by centrifuging the mixture, washed with cyclohexane and absolute ethanol (1:4) many times, and then dried in vacuum for further characterization.

Synthesis of Co 4-atom-thick layers. In a typical procedure, 100 mg $Co(acac)_3$ was added into a solution of 20 ml dimethylformamide, 4 ml H_2O and 1 ml *n*-butylamine. After vigorous stirring for 15 min, the mixture was transferred into a 40-ml Teflon-lined autoclave (before this experiment, the autoclave was initially treated with 20 ml *n*-butylamine at 120 °C for 6 h, and then treated with 35 ml H_2O at 120 °C for 12 h), sealed and heated at 220 °C for 48 h. The system was allowed to cool down to room temperature naturally, and the final product was collected by centrifuging the mixture, washed with cyclohexane and absolute ethanol (1:4) many times, and then dried in vacuum for further characterization.

Synthesis of partially oxidized bulk Co. In a typical procedure, 1.0 g $CoCl_2{\cdot}6H_2O$ was added into a solution of 15 ml ethylene glycol and 15 ml ethylenediamine. After vigorous stirring for 15 min, the mixture was transferred into a 40-ml Teflon-lined autoclave, sealed and heated at 220 °C for 12 h. The system was allowed to cool down to room temperature naturally, and the final product was collected by centrifuging the mixture, washed with cyclohexane and absolute ethanol (1:4) many times, and then dried in vacuum for further characterization.

Synthesis of bulk Co. In a typical procedure, 1.0 g $CoCl_2{\cdot}6H_2O$ was added into a solution of 15 ml ethylene glycol and 15 ml ethylenediamine. After vigorous stirring for 15 min, the mixture was transferred into a 40-ml Teflon-lined autoclave, sealed and heated at 220 °C for 24 h. The system was allowed to cool down to room temperature naturally, and the final product was collected by centrifuging the mixture, washed with cyclohexane and absolute ethanol (1:4) many times, and then dried in vacuum for further characterization.

Characterization. The field emission scanning electron microscope (SEM) images were performed by using a FEI Sirion-200 SEM. XRD patterns were recorded by using a Philips X'Pert Pro Super diffractometer with Cu Kα radiation ($\lambda = 1.54178$ Å). Atomic force microscopy in the present work was performed using a Veeco DI Nano-scope MultiMode V system. The TEM was carried out on a JEM-2100F field emission electron microscope at an acceleration voltage of 200 kV. The high-resolution TEM, HAADF-STEM and the corresponding energy dispersive spectroscopy mapping analyses were performed on a JEOL JEM-ARM200F TEM/STEM with a spherical aberration corrector. Raman spectra were detected on a RenishawRM3000 Micro-Raman system.

Electrochemical measurements. Electrochemical measurements were carried out in a three-electrode system at an electrochemical station (CHI760E). Typically, a 10-mg sample and 40 μl of Nafion solution (5 wt%) were dispersed in 1 ml of water–ethanol solution with a volume ratio of 3:1 by sonicating for 1 h to form a homogeneous ink. Then, 30 μl of the dispersion was loaded onto a glassy carbon electrode with diameter 12 mm. For CO_2 reduction experiments, linear sweep voltammetry with a scan rate of 20 mV s^{-1} was conducted in CO_2-saturated 0.1 M Na_2SO_4 solution (60 ml, pH ≈ 6) (the Na_2SO_4 electrolyte was purged with CO_2 for 30 min before the measurement). For comparison, linear sweep voltammetry with a scan rate of 20 mV s^{-1} was also conducted in N_2-saturated 0.1 M Na_2SO_4 solution. The glassy carbon electrode served as the working electrode. The counter and the reference electrodes were the platinum gauze and the SCE reference electrode, respectively. The liquid products were quantified by NMR (Bruker AVANCE AV III 400) spectroscopy, in which 0.5 ml electrolyte was mixed with 0.1 ml D_2O (deuterated water) and 0.05 μl dimethyl sulfoxide (DMSO, Sigma, 99.99%) was added as an internal standard. The one-dimensional ^1H spectrum was measured with water suppression using a pre-saturation method. The evolved gas products were detected using an Agilent Technologies 7890B gas chromatograph.

ECSA = $R_f S$, in which S stands for the real surface area of the smooth metal electrode, which was generally equal to the geometric area of glassy carbon electrode (in this work, $S = 1.13$ cm^{-2}). The roughness factor R_f was estimated from the ratio of double-layer capacitance C_{dl} for the working electrode and the corresponding smooth metal electrode (assuming that the average double-layer capacitance of a smooth metal surface is 20 μF cm^{-2})[25], that is, $R_f = C_{dl}/20\,\mu F\,cm^{-2}$. The C_{dl} was determined by measuring the capacitive current associated with double-layer charging from the scan-rate dependence of cyclic voltammetric stripping. For this, the potential window of cyclic voltammetric stripping was −0.3 V to −0.2 V versus SCE (0.1 M Na_2SO_4 solution). The scan rates were 20 mV s^{-1}, 30 mV s^{-1}, 50 mV s^{-1}, 80 mV s^{-1}, 100 mV s^{-1} and 120 mV s^{-1}. The C_{dl} was estimated by plotting the $\Delta j = (j_a - j_c)$ at −0.25 V (where j_c and j_a are the cathodic and anodic current densities, respectively) versus SCE against the scan rate, in which the slope was twice that of C_{dl}. ECSA-corrected Tafel slopes for formate production (that is, $j_{total} \times \eta_{formate}$/ECSA) were calculated from the corresponding ECSA-corrected current densities for formate according to the linear sweep voltammetry curves and the formate Faradaic efficiency ($\eta_{formate}$). The Faradaic efficiency of formate was calculated from the total amount of charge Q (in units of coulombs) passed through the sample and the total amount of formate produced $n_{formate}$ (in moles). $Q = I \times t$, where I (in amperes) is the reduction current at a specific applied potential and t is the time (in seconds) for the constant reduction current. The total amount of formate produced was measured using NMR (Bruker AVANCE AV III 400) spectroscopy. Assuming that two electrons are needed to produce one formate molecule, the Faradaic efficiency can be calculated as follows: Faradaic efficiency $= 2F \times n_{formate}/Q = 2F \times n_{formate}/(I \times t)$, where F is the Faraday constant.

25. Popczyk, M., Serek, A & Budniok, A. Production and properties of composite layers based on an Ni–P amorphous matrix. *Nanotechnology* **14,** 341–346 (2003).

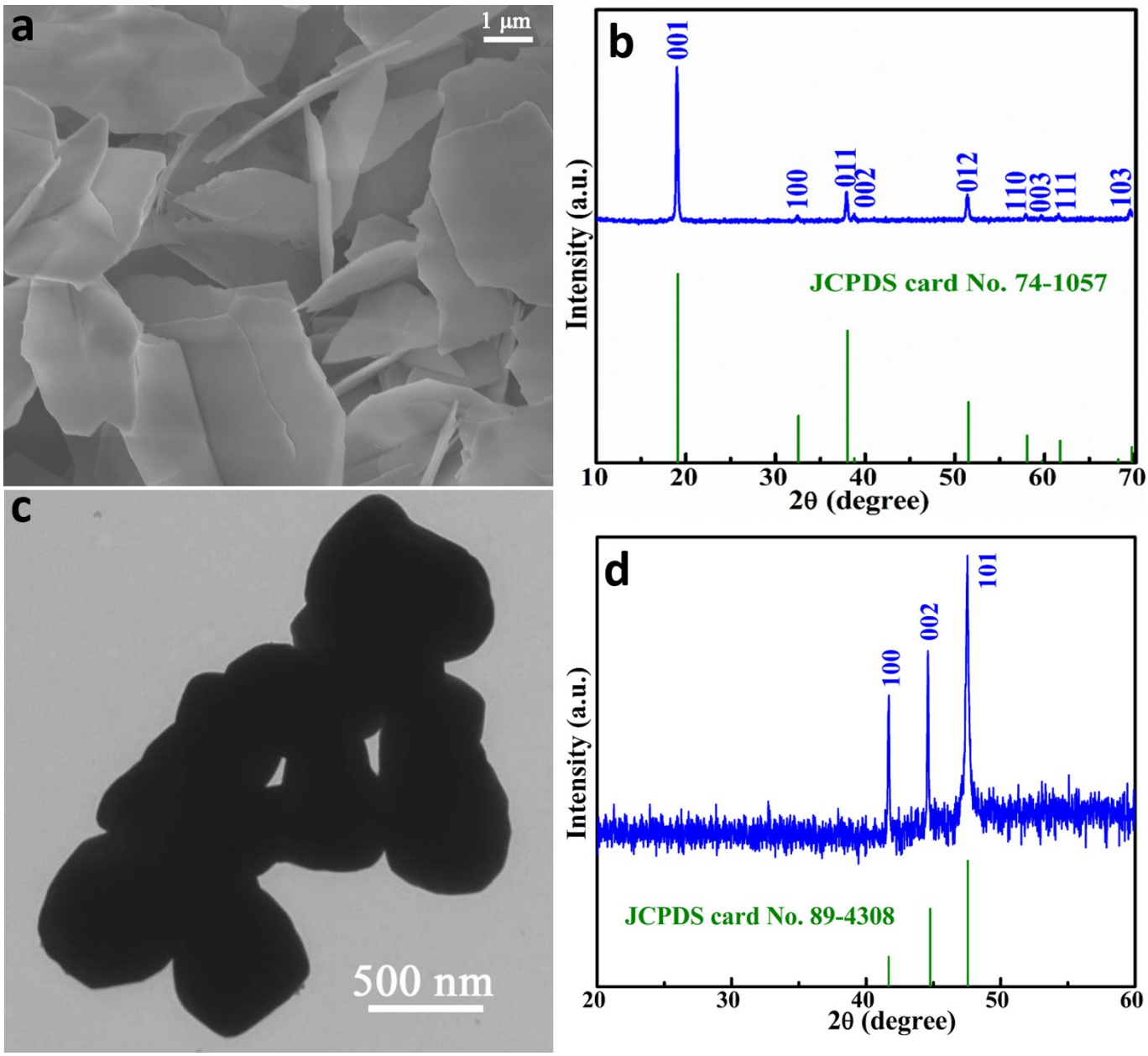

Extended Data Figure 1 | Characterizations for the comparable products. a, **b**, SEM image (**a**) and XRD pattern (**b**) for $Co(OH)_2$ sheets. **c**, **d**, TEM image (**c**) and XRD pattern (**d**) for large and irregular Co particles. In the case where only *n*-butylamine was present, the reaction produced two-dimensional $Co(OH)_2$ sheets (**a**, **b**), whereas the reaction yielded large and irregular Co particles when only dimethylformamide was used (**c**, **d**). These results indicated that *n*-butylamine favoured the formation of a sheet-like morphology, while dimethylformamide was beneficial in reducing the cobalt ions with high oxidation states. JCDPS, the Joint Committee on Powder Diffraction Standards.

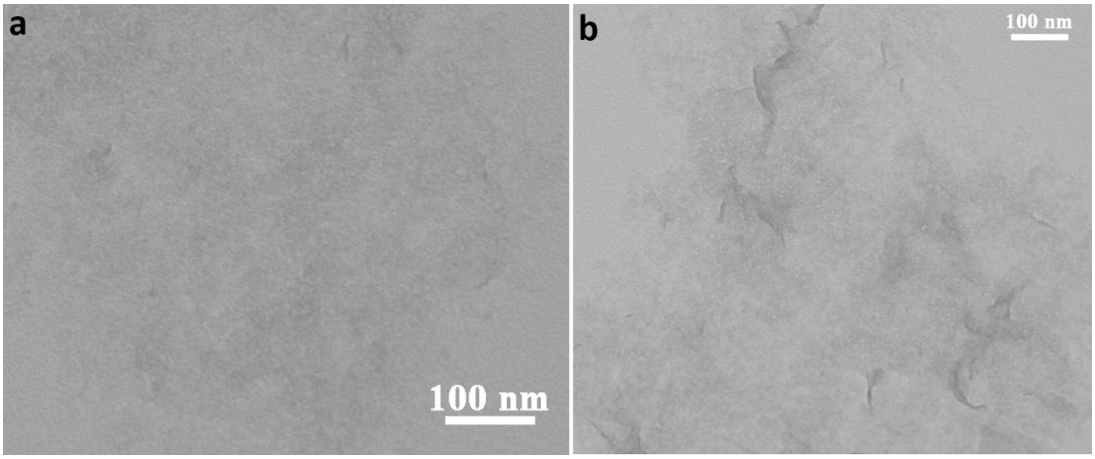

Extended Data Figure 2 | Characterizations for the intermediate products. TEM images for the obtained products at 220 °C for 0.5 h (**a**) and 2 h (**b**).

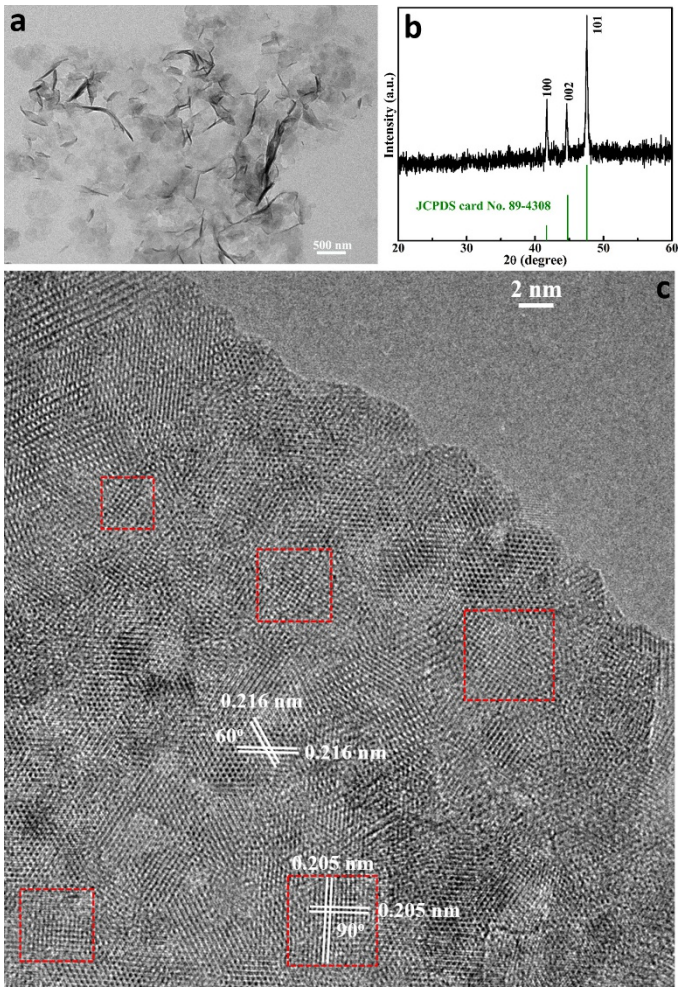

Extended Data Figure 3 | Supplementary characterizations for the partially oxidized Co 4-atom-thick layers. a, TEM image. **b**, XRD pattern. **c**, High-resolution TEM image, in which the majority of these two-dimensional sheets corresponds to the [001]-oriented hexagonal Co, while the other structural domains denoted by red squares correspond to the cubic Co_3O_4.

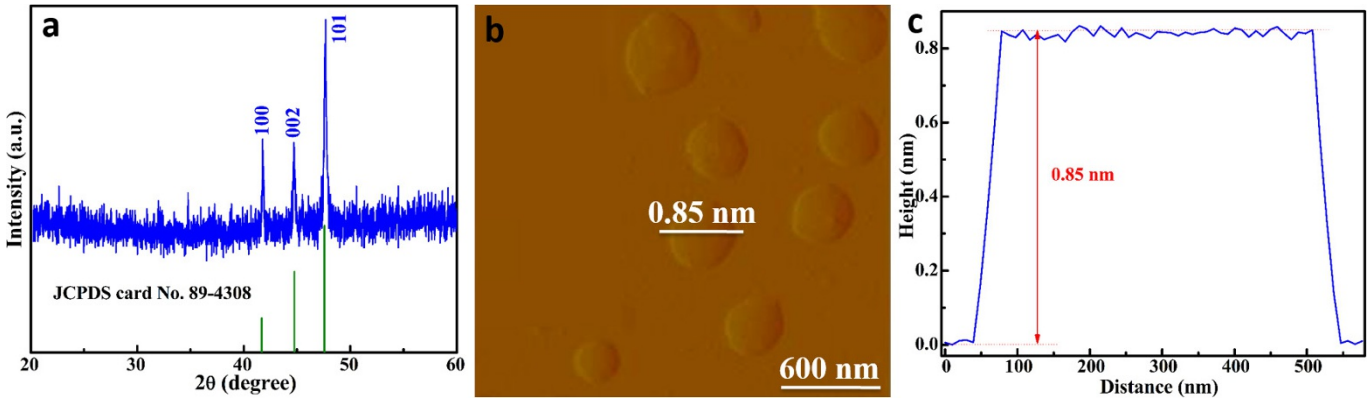

Extended Data Figure 4 | Characterizations for the Co 4-atom-thick layers. a, XRD pattern. **b**, Atomic force microscope image. **c**, The corresponding height profile. Data are shown for the products obtained at 220 °C for 48 h.

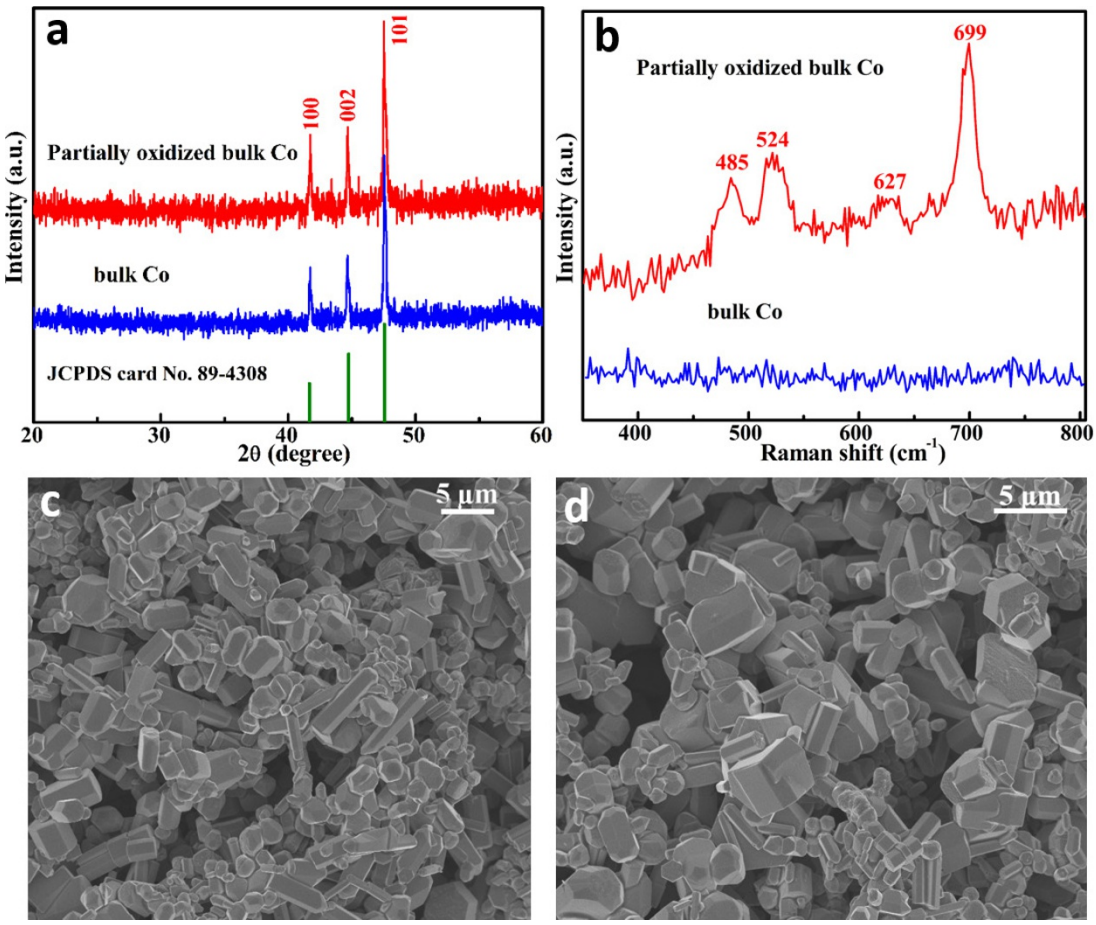

Extended Data Figure 5 | Characterizations for partially oxidized bulk Co and bulk Co particles. a, XRD patterns. **b**, Micro-Raman spectra. **c**, SEM image for partially oxidized bulk Co particles. **d**, SEM image for bulk Co particles.

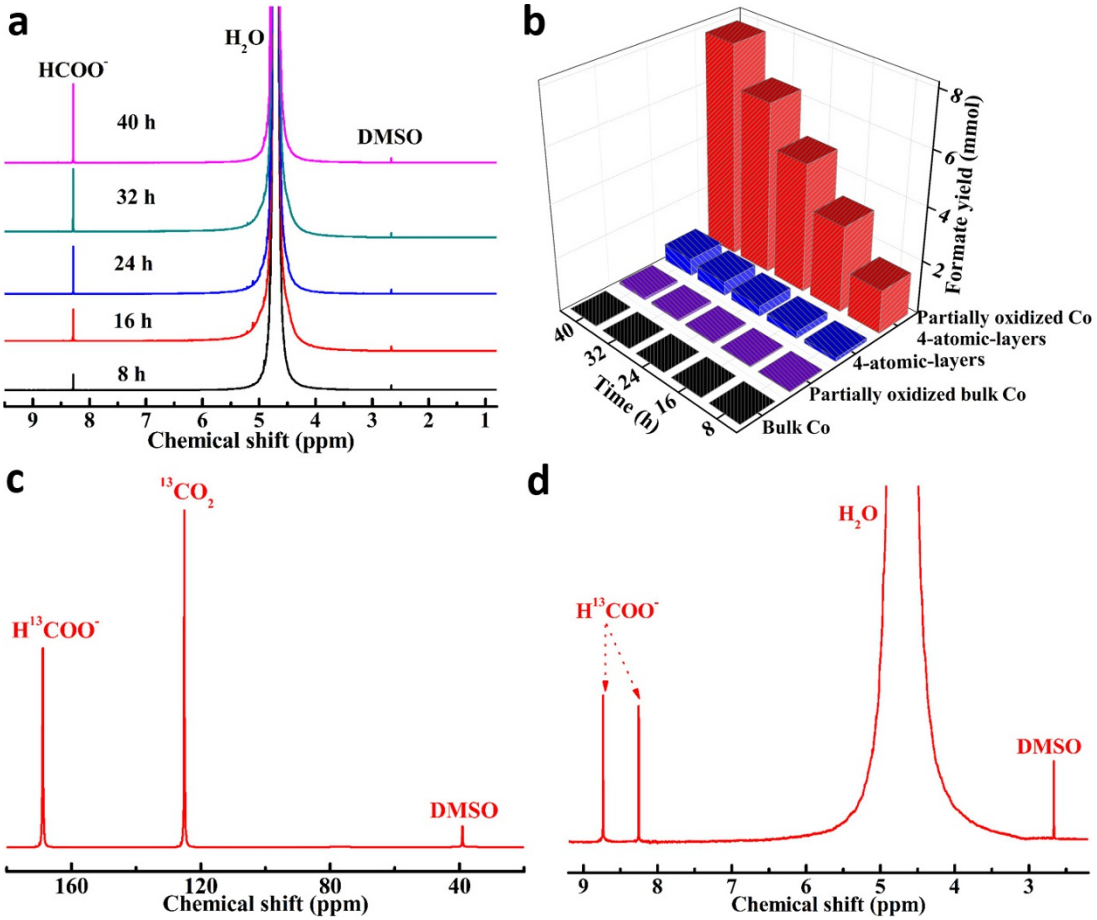

Extended Data Figure 6 | NMR spectra and formate yield. **a**, Representative NMR spectra of the electrolyte after CO_2 reduction electrolysis at −0.85 V versus SCE for the partially oxidized Co 4-atom-thick layers. DMSO is used as an internal standard for quantification of $HCOO^-$. **b**, Formate yield at the corresponding potentials with the highest Faradaic efficiencies for the partially oxidized Co 4-atom-thick layers, pure Co 4-atom-thick layers, partially oxidized bulk Co and bulk Co. Independently prepared electrodes evaluated under identical conditions in **b** exhibited a variability of <10% for the formate yield. **c**, **d**, ^{13}C spectra (**c**) and ^{1}H-NMR spectra (**d**) of the electrolyte after 8 h $^{13}CO_2$ reduction electrolysis at −0.85 V versus SCE for the partially oxidized Co 4-atom-thick layers.

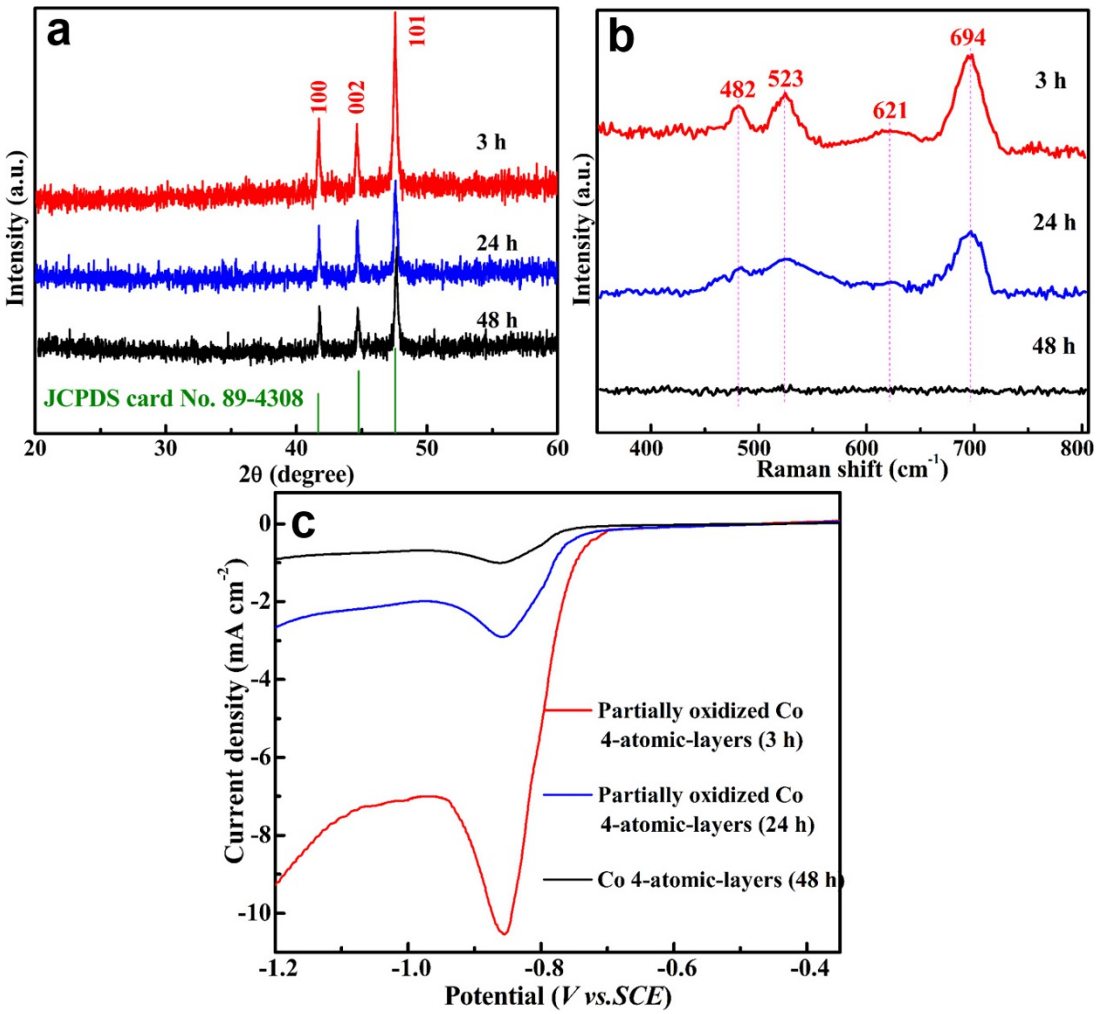

Extended Data Figure 7 | Comparison for Co 4-atom-thick layers in the absence or presence of cobalt oxide with different concentrations. **a**, XRD patterns. **b**, Raman spectra. **c**, Linear sweep voltammetric curves. Data are for a CO_2-saturated 0.1 M Na_2SO_4 aqueous solution for the partially oxidized Co 4-atom-thick layers obtained at 220 °C for 3 h, partially oxidized Co 4-atom-thick layers obtained at 220 °C for 24 h (the synthesis process is the same as that for fabricating the partially oxidized Co 4-atom-thick layers obtained at 220 °C for 3 h except that the synthetic time is increased from 3 h to 24 h; note that the increased reaction time results in the decreased amount of cobalt oxide in the Co 4-atom-thick layers), and pure Co 4-atom-thick layers obtained at 220 °C for 48 h.

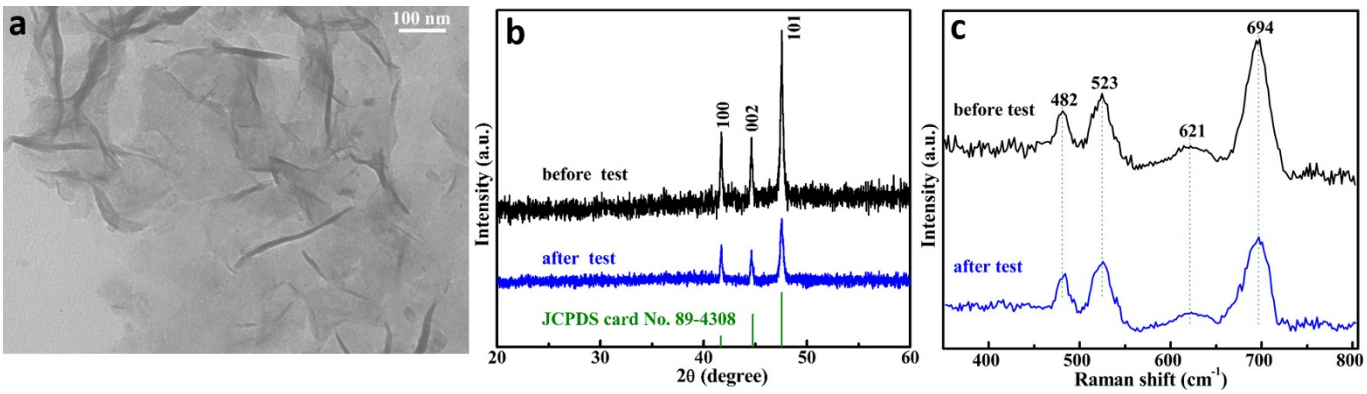

Extended Data Figure 8 | Characterizations for the partially oxidized Co 4-atom-thick layers after the 40-h test. a, TEM image for the partially oxidized Co 4-atom-thick layers after the 40-h CO_2 reduction test. **b**, **c**, XRD patterns (**b**) and Raman spectra (**c**) for the partially oxidized Co 4-atom-thick layers before and after the 40-h CO_2 reduction test. The samples for the above characterizations were collected as follows: the working electrodes after 40 h of electrolysis were sonicated in ethanol for about 3 min and then the samples were collected by centrifuging the mixture, washed with cyclohexane and absolute ethanol (1:4) many times, and then dried in vacuum. The above process was performed on approximately 50 similar working electrodes and all the samples collected were used to conduct the above characterizations.

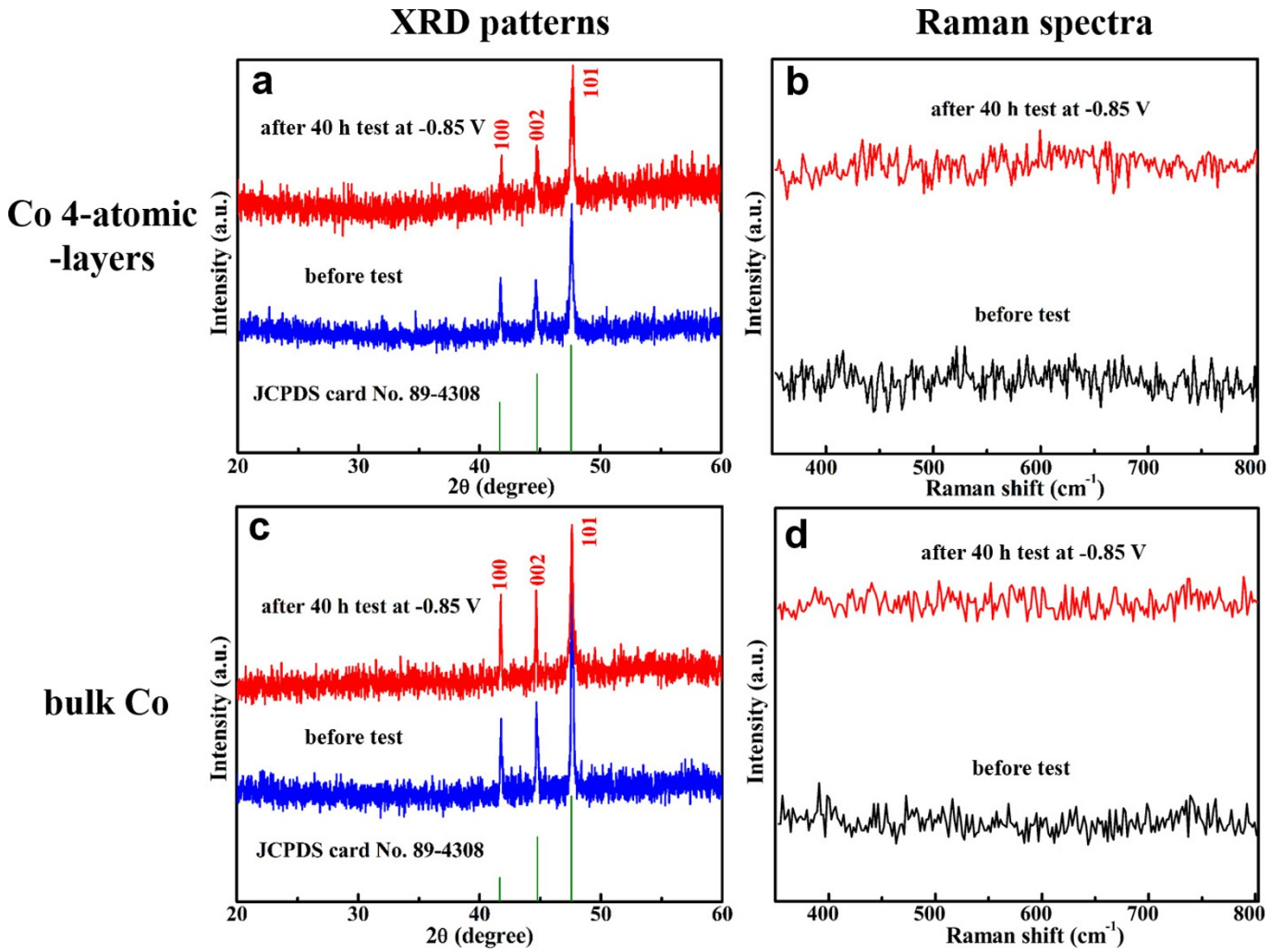

Extended Data Figure 9 | XRD patterns and Raman spectra before and after 40-h electrolysis at −0.85 V versus SCE for Co 4-atom-thick layers and bulk Co. a, **b**, XRD patterns (**a**) and Raman spectra (**b**) for Co 4-atom-thick layers. **c**, **d**, XRD patterns (**c**) and Raman spectra (**d**) for bulk Co.

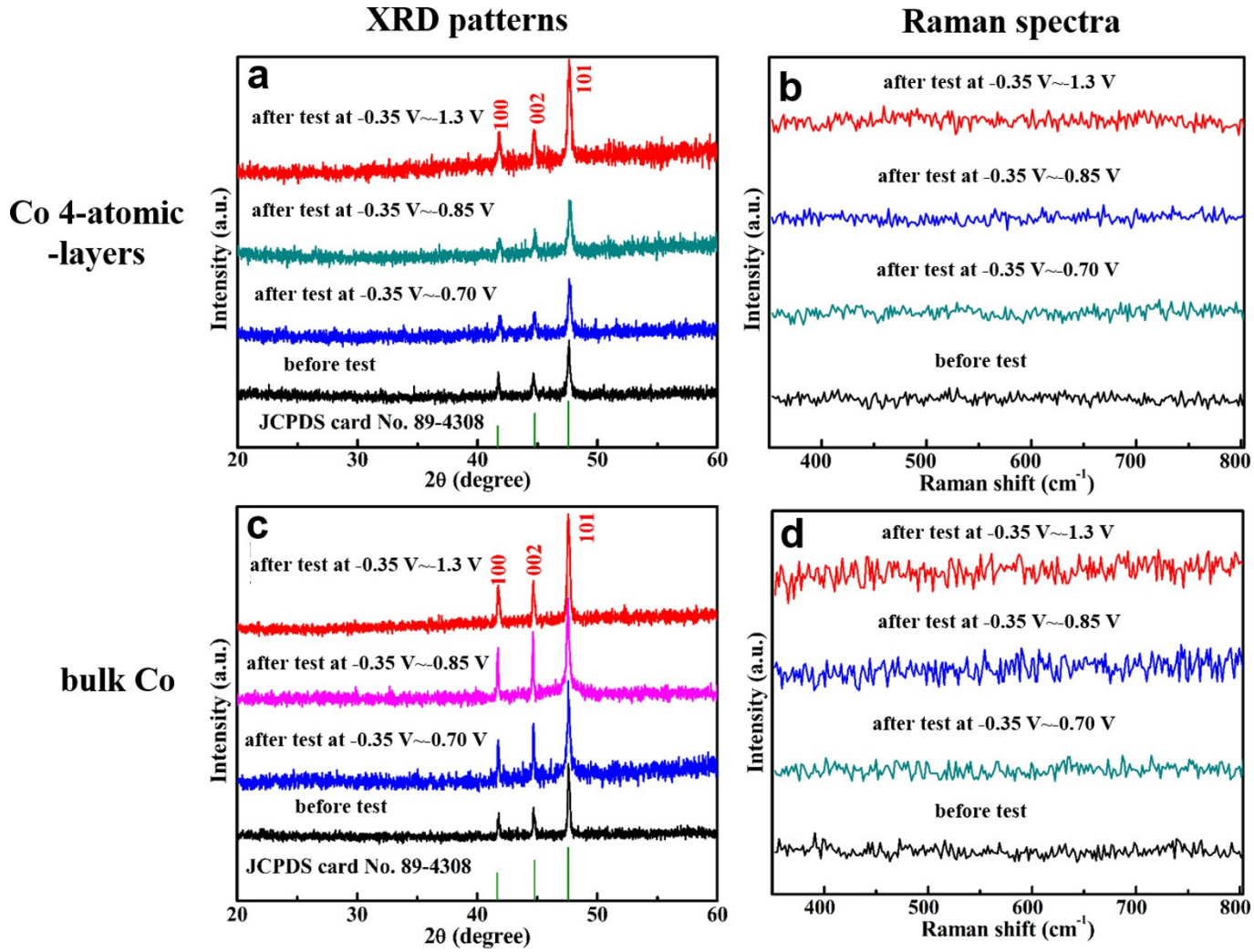

Extended Data Figure 10 | XRD patterns and Raman spectra before and after repeating linear sweep voltammetry measurement scanning from −0.35 V versus SCE to different potentials (versus SCE) about 300 times. a, **b**, XRD patterns (**a**) and Raman spectra (**b**) for Co 4-atom-thick layers. **c**, **d**, XRD patterns (**c**) and Raman spectra (**d**) for bulk Co.